POLITECNICO DI TORINO
Repository ISTITUZIONALE

Effects of anisotropy and infill pattern on compression properties of 3D printed CFRP: mechanical analysis and elasto-plastic finite element modelling

Original
Effects of anisotropy and infill pattern on compression properties of 3D printed CFRP: mechanical analysis and elasto-plastic finite element modelling / Bandinelli, F., Scapin, M., Peroni, L.. - In: RAPID PROTOTYPING JOURNAL. - ISSN 1355-2546. - ELETTRONICO. - 30:11(2024), pp. 142-158. [10.1108/RPJ-11-2023-0385]

Availability:
This version is available at: 11583/2990354 since: 2024-07-04T08:49:08Z

Publisher:
Emerald Publishing

Published
DOI:10.1108/RPJ-11-2023-0385

Terms of use:

This article is made available under terms and conditions as specified in the corresponding bibliographic description in the repository

Publisher copyright

(Article begins on next page)

28 November 2026

Effects of anisotropy and infill pattern on compression properties of 3D printed CFRP: mechanical analysis and elasto-plastic finite element modelling

Francesco Bandinelli, Martina Scapin and Lorenzo Peroni
Department of Mechanical and Aerospace Engineering, Politecnico di Torino, Turin, Italy

Abstract

Purpose – Finite element (FE) analysis can be used for both design and verification of components. In the case of 3D-printed materials, a proper characterization of properties, accounting for anisotropy and raster angles, can help develop efficient material models. This study aims to use compression tests to characterize short carbon-reinforced PA12 made by fused filament fabrication (FFF) and to model its behaviour by the FE method.

Design/methodology/approach – In this work, the authors focus on compression tests, using post-processed specimens to overcome external defects introduced by the FFF process. The material's elastoplastic mechanical behaviour is modelled by an elastic stiffness matrix, Hill's anisotropic yield criterion and Voce's isotropic hardening law, considering the stacking sequence of raster angles. A FE analysis is conducted to reproduce the material's compressive behaviour through the LS-DYNA software.

Findings – The proposed model can capture stress values at different deformation levels and peculiar aspects of deformed shapes until the onset of damage mechanisms. Deformation and damage mechanisms are strictly correlated to orientation and raster angle.

Originality/value – The paper aims to contribute to the understanding of 3D-printed material's behaviour through compression tests on bulk 3D-printed material. The methodology proposed, enriched with an anisotropic damage criterion, could be effectively used for design and verification purposes in the field of 3D-printed components through FE analysis.

Keywords Anisotropy, Composite materials, Finite element analysis, Material properties

Paper type Research paper

1. Introduction

Short fibre-reinforced polymer composites represent an interesting class of materials, combining the lightweight and ductility properties of the polymeric matrix with the high load-bearing capability of several types of fibres (Tekinalp *et al.*, 2014; Ning *et al.*, 2015; Zhang *et al.*, 2018; Khan *et al.*, 2021). One of the most used additive manufacturing techniques is fused filament fabrication (FFF) (Turner *et al.*, 2014; Turner *et al.*, 2014; Bikas *et al.*, 2016; Wickramasinghe *et al.*, 2020), where the component is built layer by layer through the direct deposition of fused material through a heated nozzle. Despite its popularity, there is still much work needed to fully understand the mechanical behaviour of FFF components, and the characterization of printed materials is an ongoing process (Zhao *et al.*, 2019; Yao *et al.*, 2020; Fang *et al.*, 2021; Scapin *and* Peroni, 2021; Zouaoui *et al.*, 2021; Athale *et al.*, 2022; Bandinelli *et al.*, 2023).

The building strategy of the FFF process introduces peculiar aspects of the printed material, among which mechanical anisotropy is the most relevant. The printing process is based on the deposition of fused material on a printing bed, where the nozzle moves combining translations along X and Y directions (as shown in Figure 1), and the vertical growth of the component is assured by the bed motion along the Z direction, which creates the characteristic layers. The poor adhesion between different layers and different rasters makes the material inhomogeneous, creating weak interfaces and voids that play a fundamental role in defining the mechanical behaviour of the whole structure (Zhang *et al.*, 2018; Sood *et al.*, 2009; Fallon *et al.*, 2019; Birosz *et al.*, 2022). As already observed in many past works (Ziemian *et al.*, 2012; Garg and Bhattacharya, 2016; Dudescu and Racz, 2017; Gonabadi *et al.*, 2020; Calignano *et al.*, 2020), the weakest direction in terms of tensile properties is the growth direction of the print (Z

The current issue and full text archive of this journal is available on Emerald Insight at: **https://www.emerald.com/insight/1355-2546.htm**



Rapid Prototyping Journal
30/11 (2024) 142–158
Emerald Publishing Limited [ISSN 1355-2546]
[DOI 10.1108/RPJ-11-2023-0385]

© Francesco Bandinelli, Martina Scapin and Lorenzo Peroni. Published by Emerald Publishing Limited. This article is published under the Creative Commons Attribution (CC BY 4.0) licence. Anyone may reproduce, distribute, translate and create derivative works of this article (for both commercial and non-commercial purposes), subject to full attribution to the original publication and authors. The full terms of this licence may be seen at http://creativecommons.org/licences/by/4.0/legalcode

The authors would like to thank FiberForce for providing the printing materials. The research used the equipment of DYNLab Laboratory at Politecnico di Torino co-funded by POR FESR Piemonte 2014–2020.

Received 3 November 2023
Revised 22 March 2024
Accepted 19 April 2024

Figure 1 Representation of the printing process in the reference system of the printer

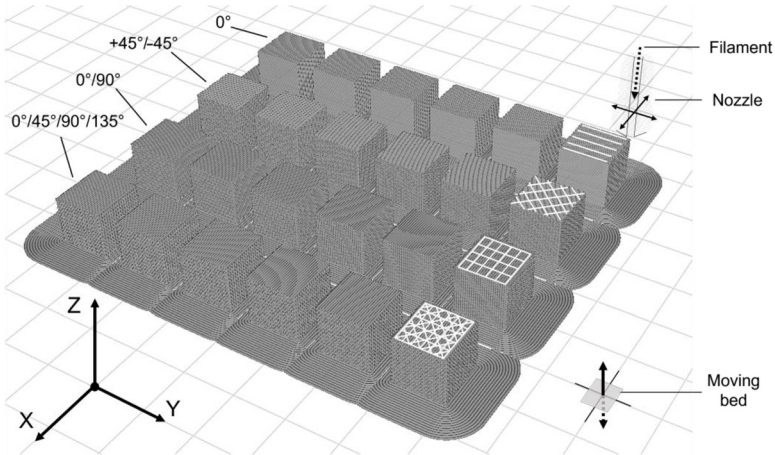

Notes: Each horizontal row has a different stacking sequence of raster angles (shown in white continuous lines) and two specimens to be tested in the principal directions of the printer reference system
Source: Figure by authors

direction), because of poor adhesion. The lateral interface between rasters is also a critical aspect of the material's integrity; in fact, the newly fused material is deposited in a later stage with respect to the previously deposited one, with a time delay that depends on the printing speed and strategy (Sun, 2008; Sood *et al.*, 2012; Samy *et al.*, 2022). Material adhesion depends on many printing parameters as well as material properties such as viscosity and wettability. In the case of fibre-reinforced materials, the bonding between two distinct portions of material is particularly critical because of the presence of fibres in the matrix that enhance discontinuity and increase the viscosity (Zhang *et al.*, 2018; Fallon *et al.*, 2019). Many authors focused on the characterization of tensile properties with particular attention to the effects of material orientation and raster angle, observing a relevant influence of both parameters on the material's anisotropy (Zhao *et al.*, 2019; Yao *et al.*, 2020; Zouauoi *et al.*, 2021; Bandinelli *et al.*, 2023; Dudescu and Racz, 2017; Gonabadi *et al.*, 2020; Guessasma *et al.*, 2016; Kannan *et al.*, 2020; Zeybek *et al.*, 2023). Generally, tensile testing is the most used material characterization method to find the elastic modulus, yield and ultimate tensile strengths. Especially in the case of anisotropic materials, tensile tests could be insufficient to fully understand the mechanical behaviour, as different deformation and failure modes could be involved depending on the nature of the load applied. With the aim of complete material characterization, compression tests on bulk FFF materials should be considered along with tensile ones, but only some works focus on this type of testing to obtain the material's properties (Athale *et al.*, 2022; Sood *et al.*, 2012; Guessasma *et al.*, 2016; Zeybek *et al.*, 2023; Song *et al.*, 2017; Tabacu and Ducu, 2020; Corvi *et al.*, 2023; Peng *et al.*, 2022). Athale *et al.* (2022) focused on the characterization of PA12 with short carbon fibres, observing a neat difference between tensile and compression properties. Zeybek *et al.* (2023) focused on PA6 with short carbon fibres, obtaining a dependency of compression properties on the strain rate of deformation. Among previous works, to the best of the authors' knowledge, only a few use compression properties of FFF materials to represent their compressive behaviour using finite element (FE) models (Athale *et al.*, 2022; Guessasma *et al.*, 2016; Song *et al.*, 2017; Tabacu and Ducu, 2020; Corvi *et al.*, 2023). The present work has the objective of characterizing and modelling the compressive behaviour of an FFF-printed composite material, made of a polyamide matrix (PA12) and reinforced with short carbon fibres, using compression tests on cubic specimens built with different orientations in space and different stacking sequences of raster angles. Compression tests are used to evaluate both elastic and plastic properties, and obtained data are subsequently used to define a material model that describes the elastic regime, the transition between the elastic and the plastic regime and, finally, the evolution in the plastic regime, before the onset of damage mechanisms. Plastic deformation mechanisms are fundamental for a complete understanding of 3D-printed polymers' behaviour, especially when dealing with the design of components, failure analysis and design of manufacturing processes (Bandinelli *et al.*, 2024). Hence, the present work is particularly focused on the plastic behaviour of 3D-printed materials and a possible strategy for its modelling. The final scope of this work is demonstrating the possibility of using FE calculation methods as design and verification tools for this special class of materials. The present work adopts a commercial FE software named LS-DYNA (Livermore Software Technology Corporation (LSTC), 2012), as well as a correlated optimization software named LS-OPT (Stander *et al.*, 2019).

2. Materials and methods

The material analysed in the present work is Nylforce Carbon produced by FiberForce (Treviso, Italy) composed of a nylon matrix (PA12) reinforced with short carbon fibres (20% Wt.) and characterized by significant mechanical properties, low density

(1 g/cm^3) and resistance to high temperatures (long term at 90° C–120°C and short term at 150°C). Previous work by the authors on the same material showed a strong anisotropic nature in tensile conditions. Specimens printed with a ±45° raster angle with a 0° orientation with respect to the printing bed exhibited an ultimate tensile load of 35 MPa, whereas specimens with a 90° orientation with respect to the printing bed exhibited a much lower 16 MPa (Bandinelli *et al.*, 2023).

For the present work, specimens are printed with a cubic shape, with a final side dimension of 10 mm. The slicer software used for the specimen's preparation is Cura Slicer (version 5.2.1). The printer used is the Ultimaker S5 (Ultimaker B.V., Utrecht, NL) with a 0.4 mm Olsson ruby nozzle (3DVerkstan, Stockholm, Sweden). The filament used is produced by FiberForce with a diameter of 2.85 mm. The printing parameters are adjusted to have the optimal results in terms of geometrical accuracy, raster bonding and layer adhesion. In this sense, the printing temperature is set to 270° C, the printing chamber is enclosed and heated through an electrical resistance and a fan to maintain a temperature of 80° C, material's flow rate is raised to 120% of its default value and the printing speed is set to 40 mm/s while layer height is set to 0.2 mm. These changes enhance raster bonding and layer adhesion, as the material has a longer cooling time, promoting better chemical and physical adherence between material deposited in different moments of the print. Longer cooling time promotes the crystallization of the polymeric matrix, increasing mechanical performances (Calignano *et al.*, 2020; Ferreira *et al.*, 2020; Yu *et al.*, 2023). Furthermore, higher chamber temperatures promote low cooling rates and low-temperature gradients, limiting the warping of the final parts and the formation of voids (Wang *et al.*, 2007; Yu *et al.*, 2020).

As already stated in Ferrell *et al.* (2021); Ginoux *et al.* (2023); Phillips *et al* (2022); Sola *et al.* (2023), FFF material characterization is particularly difficult when dealing with the repeatability of results, because of numerous influences of different printing parameters on the final component. Furthermore, the absence of a standardized testing procedure results in obtaining different mechanical properties between various research works on the same material, highlighting the need for standardization, especially from the specimen fabrication point of view. Up to date, ASTM D695 and ASTM D1621 can be used for compression tests on plastics, although they are not intended for 3D-printed materials they provide few indications to deal with anisotropic materials. It is of fundamental importance to describe the procedure followed for the realization of test specimens, because each parameter plays a role in the result, and the FFF process involves many parameters to be controlled (Samy *et al.*, 2022; Phillips *et al.*, 2022; Chacón *et al.*, 2017).

In the present work, the experimental campaign conducted to study the mechanical behaviour of the material and to find its properties is divided into two phases: the first phase is aimed to assess the repeatability of the results and observe the influence of raster angle on the compression properties of the material; the second one is instead aimed to extend the mechanical behaviour analysis to the dependence of the material's compression properties from its orientation with respect to the load. In the latter phase, the work is focused on two stacking sequences of raster angles only: the most anisotropic (0° raster angle configuration) and the most isotropic configurations (135° raster angle configuration), based on the paths of raster deposition. This is intended to highlight differences in the behaviour of the same material. Specimens used in the present work do not follow the standards for plastic compression testing but are designed to analyse multiple manufacturing and loading cases.

2.1 Specimens tested along the main material's directions

For the first phase of the experimental campaign, specimens are realized to be tested as printed, aligning the loading directions with the main directions X, Y and Z of the printing reference system, as shown in Figure 1. Four different raster angles are analysed: the 0° configuration (in which rasters are aligned with the Y direction), the ±45° configuration, the 0°/90° configuration and, finally, the 0°/45°/90°/135° configuration. These specimens were printed in four batches consisting of 24 cubes (a total of 8 repetitions for each combination of loading direction and raster angle) to conduct a statistical analysis of the mechanical properties to evaluate the repeatability of the printing process and testing procedure. Specimens were characterized by a slight curvature of the face in contact with the build plate, showing the effects of shrinkage and warping as observed in past works (Tekinalp *et al.*, 2014; Samy *et al.*, 2022; Wang *et al.*, 2007; Ferrell *et al.*, 2021; Cattenone *et al.*, 2019; Trofimov *et al.*, 2022).

2.2 Specimens printed with various orientations between loading and material directions

For the second phase of the experimental campaign, inclined specimens are printed to investigate the effects of material orientation and anisotropy.

These specimens are realized by progressive rotations of the previous cubic samples along each of the material's main directions X, Y and Z. They are printed with the help of printing supports (made by the same material). The rotation angles considered are 15°, 30°, 45°, 60° and 75°, to have a progressive transition from one main material's direction to the other as shown in Figure 2 (Ning *et al.*, 2015), where the latter represent the endpoints of the inclined series. Specimens rotated along one axis represent the transition between the remaining two.

Figure 3 shows the orientation procedure of specimens printed with progressive inclination around the y-axis, observable in Figure 2 as the top left row of specimens. Continuous lines represent the material's layers while small arrows show the direction of the compressive load so that relative orientation between the material's directions and load direction (ζ) is visible.

Printing supports are a critical feature of 3D printing, in fact, they inevitably introduce a defective surface in the finished component as can be observed in Figure 4, especially for low angles such as in the case of 15° inclined specimens (or equivalently 75°), where the spacing of layers' profiles is more evident (Buj-Corral *et al.*, 2019). Printing on inclined supports inevitably suffers from the stair-step effect (Reddy *et al.*, 2018). This phenomenon is typical of the FFF process and leads to rasters being deposited on non-planar faces, with the result of rough and inaccurate surfaces. Furthermore, specimens Z15 and Z75 presented defective surfaces because of rasters' angle with respect to the external faces, which caused prominent ridges (right image in Figure 4).

Figure 2 The left image shows specimens used for evaluating the dependence of compression properties from material orientation with respect to the load applied; the right image shows a scheme of the rotations applied to investigate the material's anisotropy

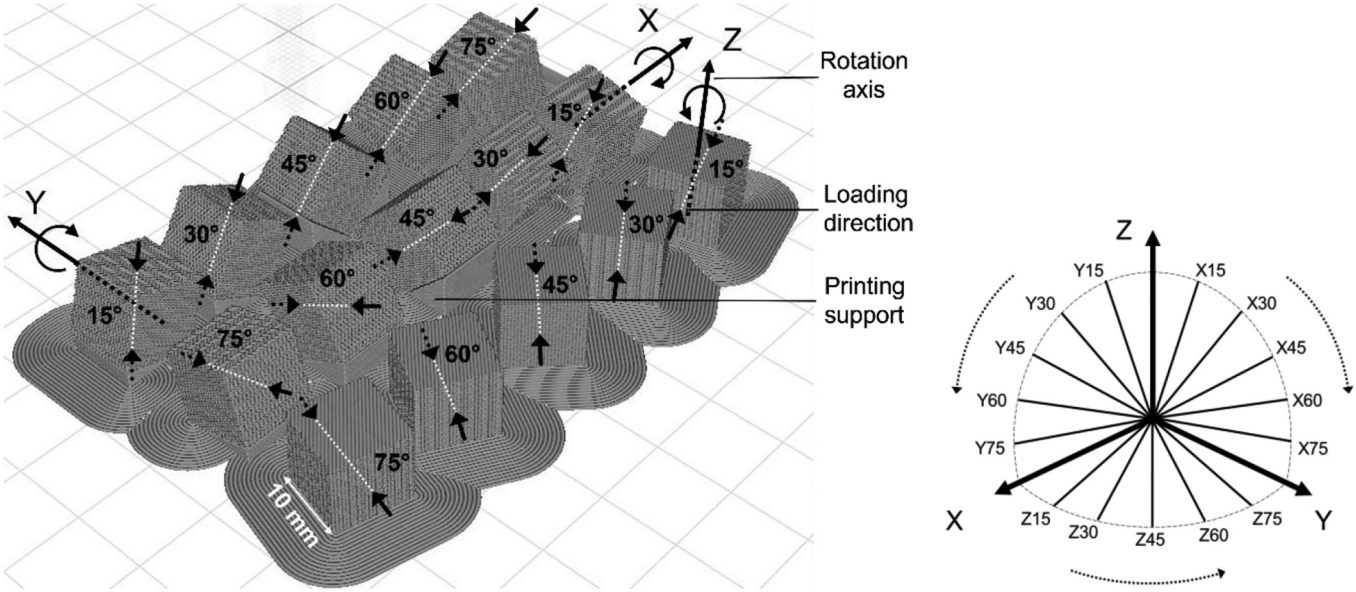

Source: Figure by authors

Figure 3 Scheme of specimens rotated around the *y*-axis, from the printing configuration with supports (top image) to the rotated configuration used for compression tests (bottom image)

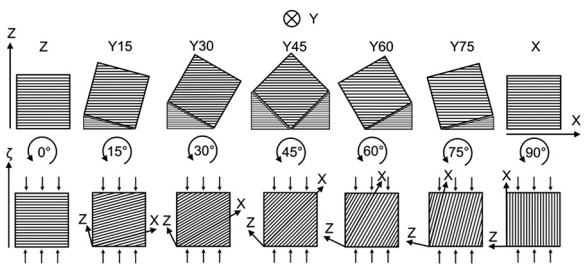

Source: Figure by authors

Considering the possible influence of the phenomena just discussed, the authors focused on a new specimen realization procedure to obtain more consistent results. Supports were replaced by bulk material, and the specimen's dimensions were augmented to 12 mm to allow post-print milling (Figure 5).

The final shape of the specimens is identical to the previously described one, having the same dimensions (side dimension of 10 mm). This procedure allows to obtain more reliable results.

2.3 Testing procedure and equipment

The test methodology involves compression tests on the cubic specimens, which are subjected to a compression load at a constant engineering strain rate of 0.01 s^{-1} until the reach of at least 50% of engineering strain, to obtain material behaviour at elevated levels of deformation. Mechanical testing is conducted with the electromechanical testing machine Zwick100 (ZwickRoell GmbH & Co. KG, Ulm, Denmark) with a 100 kN load cell. The experimental setup is completed by two PixeLINK PL-B777 cameras with 5MP resolution and equipped with a 1/2.5" sensor (PixeLINK, Ottawa, Canada) and a Tokina Macro 100 F2.8D camera lens (Kenko Tokina Co. Ltd, Tokyo, Japan). The anisotropic nature of the material analysed requires the observation of two different faces of the cubic specimens, to capture the deformation behaviour in the two directions perpendicular to that of the application of the load. Video recording was conducted through the waveform generator Lecroy WaveStation 2012 (Teledyne Lecroy, Chestnut Ridge, NY, USA), to impose an image-capturing frequency of 4 Hz. Subsequent video analysis was conducted using Tracker software (tracker.physlets.org).

3. Experimental results

The results of the compression tests are analysed evaluating stress and strain in the different printing configurations and observing the effect of both raster angle and build orientation. Data from mechanical tests are elaborated to find the mechanical properties of the material. The elastic phase is used for the evaluation of elastic modulus in the testing direction ζ (Figure 3). The next phase is the deviation of 0.2% of strain from the proportionality, which in the present work is considered as the elastic limit of the material. The transition between elastic and plastic phases is different from specimen to specimen, showing dependence on material orientation and raster angle.

3.1 Experimental results of as-printed specimens

Compression tests conducted on the as-printed specimens described in Section 2.1 show a clear effect of raster angle on the mechanical properties of the material. In Table 1 elastic moduli are reported (with standard deviations in brackets):

Figure 4 Details of X15 (left), X30 (centre) and Z75 (right) specimens, showing the effects of printing supports on the first layers deposited for the first two and the effects of the raster's path for the last one

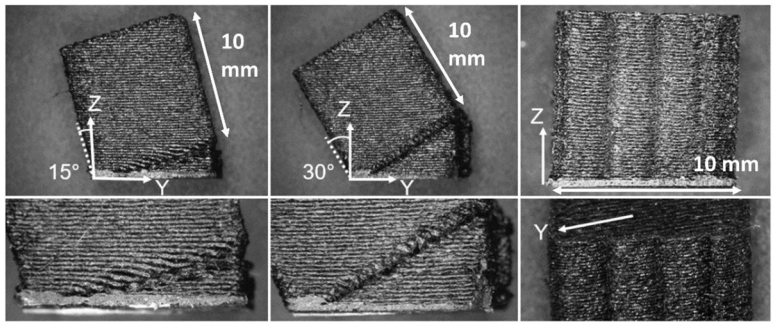

Note: Specimen X15 has considerable negative effects given by the pronounced spacing between the surfaces' edges of the support structure, as can be observed in the lower left picture
Source: Figure by authors

Figure 5 Specimens used for the second phase of the experimental campaign and detail of specimen X45, where dashed white lines delineate the contours of the post-processed specimen

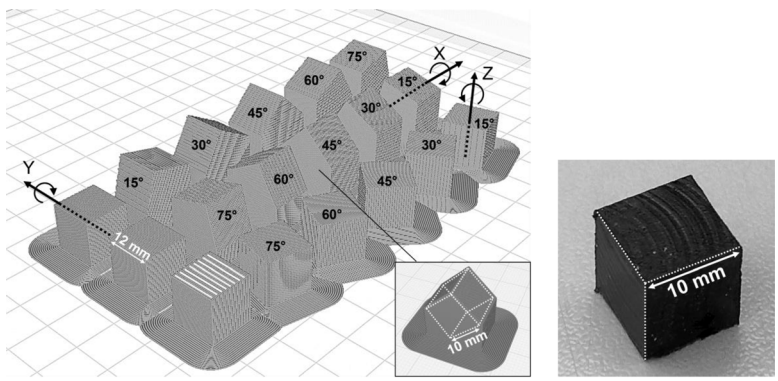

Note: The specimens depicted are printed in the 0° configuration, as shown by continuous white lines that represent rasters. The post-processed specimen is shown in the image on the right
Source: Figure by authors

Results of the compression tests on these specimens show some peculiarities that lead to the conclusion that their mechanical properties are strongly influenced by printing supports (Turner *et al.*, 2014). The results emphasize the negative impact of printing supports on elastic moduli, observed by comparing inclined specimens with those tested in the main material directions. Especially looking at the specimens between Z and X directions (from Y15 to Y75), the trend of inclined specimens is significantly lower than expected, which can be explained by the presence of printing supports (Figure 6), as they introduce a defected surface that is relatively extended with respect to the specimen's dimensions (Figure 4). Irregularities of the external surfaces induce higher deformation in earlier stages of compression, thus lowering the elastic modulus. The graphs also show that specimens inclined by 15° and 75° to the main directions are remarkably out of trend with respect to the others, especially X15, Y15 and Y75 specimens.

The 0° raster angle configuration shows the highest anisotropy, with the Y direction (coinciding with that of the deposition of the rasters) being the stiffest. This result is expected as fibres are mainly aligned with the deposition direction, so the material exhibits its maximum mechanical resistance (Tekinalp *et al.*, 2014; Heller *et al.*, 2016; Mulholland *et al.*, 2018; Tessarin *et al.*, 2022). X and Z directions of the 0° raster angle configuration show remarkably similar behaviour, with an almost identical elastic modulus. The other raster angle configurations substantially show analogous results, with material directions having perfectly comparable elastic moduli despite having different raster angles. This is because these three configurations introduce a theoretical symmetry between the X and Y directions. Compression loading in the latter configurations encounters the same orientations of rasters (and fibres) (namely, 0°, 45°, 90° and 135°) and should give comparable outputs in terms of mechanical properties. However, the experimental evidence shows a systematic difference between the X and Y directions, with X being the stiffer. This

Table 1 Elastic moduli of specimens tested as printed

Elastic modulus (MPa)	Stacking sequence			
Material direction	**0°**	**+45°/−45°**	**0°/90°**	**0°/45°/90°/135°**
X	1,021 (79)	938 (69)	953 (37)	968 (31)
Y	1,618 (57)	775 (46)	818 (31)	812 (56)
Z	986 (35)	1,181 (50)	1,172 (41)	1,178 (36)

Source: Table by authors

Figure 6 Trends of elastic moduli concerning material orientation in the case of inclined specimens tested as printed

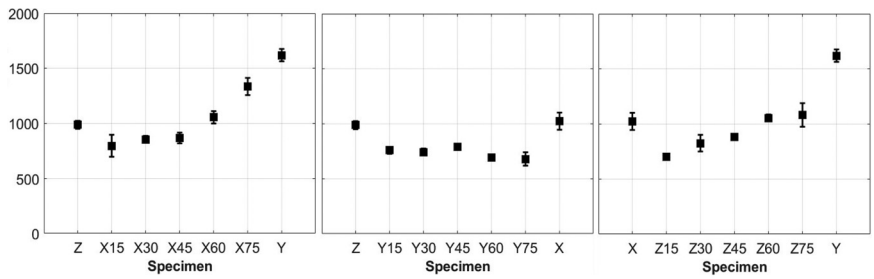

Source: Figure by authors

could be found in the warpage of the portion of the cube that is in contact with the building plate as specimens report curved bottom faces. The curvature is observed to be around the *x*-axis, so when load is applied in the Y direction the stiffness experienced is lower due to a pre-deformed configuration. Stacking sequences as +45°/−45° and 0°/90° are more subjected to warping because of higher residual stresses induced by the printing strategy, which has been shown to affect the cooling phase (Samy *et al.*, 2022; Wang *et al.*, 2007; Trofimov *et al.*, 2022). The results of these tests demonstrate that the specimens (as printed) are not completely adequate and should be post-processed to avoid the effects of warping.

3.2 Experimental results of post-processed specimens

For as the post-processed specimens are concerned, only the 0° and the 0°/45°/90°/135° configurations were tested. The authors decided to focus on these two stacking sequences to analyse the most anisotropic and the most isotropic configurations, respectively. Observing the elastic moduli obtained for the 0° raster angle configuration, it is evident that the deposition direction Y has the highest elastic modulus, due to the alignment of the load direction with that of the rasters, followed by X and Z directions that are almost comparable. This is because of the fibres' alignment during the extrusion phase (Heller *et al.*, 2016; Mulholland *et al.*, 2018; Love *et al.*, 2014). For as the elastic limit is concerned, the 0° raster angle configuration shows an analogous trend, in fact, the Y direction results in the highest value, while the Z and X directions show lower and similar values. Experimental values of the material's properties in the 0° configuration are reported in Table 2 (with standard deviation in brackets).

Where the elastic moduli E_{xx}, E_{yy}, E_{zz} and yield values Y_{xx}, Y_{yy}, Y_{zz} are identified using compression tests along the three main material's directions (X, Y and Z), whereas ν_{xy}, ν_{xz}, and ν_{yz} Poisson's ratios are derived from video analysis of transversal deformation.

The second configuration analysed has the following stacking sequence of raster angles: 0°/45°/90°/135° so that each layer is rotated by 45° with respect to the previous one. This printing strategy generates, as expected, an almost isotropic result in the printing plane (XY) in terms of elastic moduli and elastic limits, as rasters have four alternated deposition directions (Yao *et al.*, 2020; Dong *et al.*, 2017; Retolaza *et al.*, 2021). X and Y directions are stiffer than the Z direction, and the anisotropy is less noticeable with respect to the 0° configuration. Specimens tested along the main material's direction appear to behave very similarly and show analogous deformation (and failure) mechanisms: they deform almost equally along the two transverse directions (as confirmed by Poisson's ratios values) and show crack openings while being compressed. For as the elastic limit is concerned, the 0°/45°/90°/135° raster angle configuration shows remarkably similar yield values in the three main directions X, Y and Z. Experimental values of the material's properties in the 0°/45°/90°/135° configuration are reported in Table 3 (with standard deviation in brackets).

Observing the material's properties in the two different stacking sequences it is obvious to notice the effect of the raster

Table 2 Experimental values of material's properties of the specimens with 0° configuration

E_{xx} (MPa)	E_{yy} (MPa)	E_{zz} (MPa)
1393 (90)	2530 (44)	1495 (68)
ν_{xy} (−)	**ν_{xz} (−)**	**ν_{yz} (−)**
0.115 (0.013)	0.400 (0.021)	0.250 (0.018)
Y_{xx} (MPa)	**Y (MPa)**	**Y_{zz} (MPa)**
41.58 (1.72)	54.81 (0.95)	41.96 (0.80)

Source: Table by authors

angle on the final printed material. This single parameter changes the distribution of the material's stiffness in its directions, affecting its anisotropy. This suggests that raster angle is a fundamental choice for design purposes and should be selected with regard to the final application in a similar fashion as in laminate composites, where fibre orientation plays a crucial role.

4. Modelling methodology

The printing process is accurately represented by a reference system based on three axes: X, Y and Z (as shown in Figure 1) (Paul, 2021). The modelling methodology considers the directionality of the material's behaviour and will be treated accordingly.

Table 3 Experimental values of material's properties of specimens with 0°/45°/90°/135° configuration

E_{xx} (MPa)	E_{yy} (MPa)	E_{zz} (MPa)
1,679 (178)	1,761 (105)	1,530 (133)
ν_{xy} (−)	ν_{xz} (−)	ν_{yz} (−)
0.320 (0.023)	0.400 (0.027)	0.400 (0.019)
Y_{xx} (MPa)	Y_{yy} (MPa)	Y_{zz} (MPa)
42.27 (1.65)	41.01 (2.06)	39.04 (2.01)

Source: Table by authors

Tests on specimens with different orientations in space provide valuable information on the dependence of elastic and plastic properties from relative orientation between material (X, Y and Z) and loading directions (ζ) (as shown in Figure 7), giving an insight into the characteristic anisotropy of printed materials (Guessasma *et al.*, 2016; Zeybek *et al.*, 2023). Also, the latter type of test increases the number of experimental information about the mechanical behaviour of the material, strengthening considerations and reliability of the trends observed. Compression tests only conducted along the main material's directions cannot give a complete overview of the characteristic anisotropy of FFF materials and should then always come along with those where loading and material's directions do not coincide. This allows for an appropriate consideration of the behaviour of the material, especially when dealing with shear stress acting between printed layers. Shear tests are difficult to perform, and the evaluation of shear elastic and plastic properties can be conducted by uniaxial tests on inclined specimens (Bandinelli *et al.*, 2023).

4.1 Numerical modelling

Composite materials for 3D printing, such as the one analysed in this paper, show an almost linear elastic behaviour in the region of small deformations, followed by a plastic behaviour for larger deformations. For these reasons, it is plausible to consider a material model based on an elastic stiffness matrix for the

Figure 7 Scheme representing the orientation of specimens during fabrication (on the left) and testing (on the right) in the 0° printing configuration

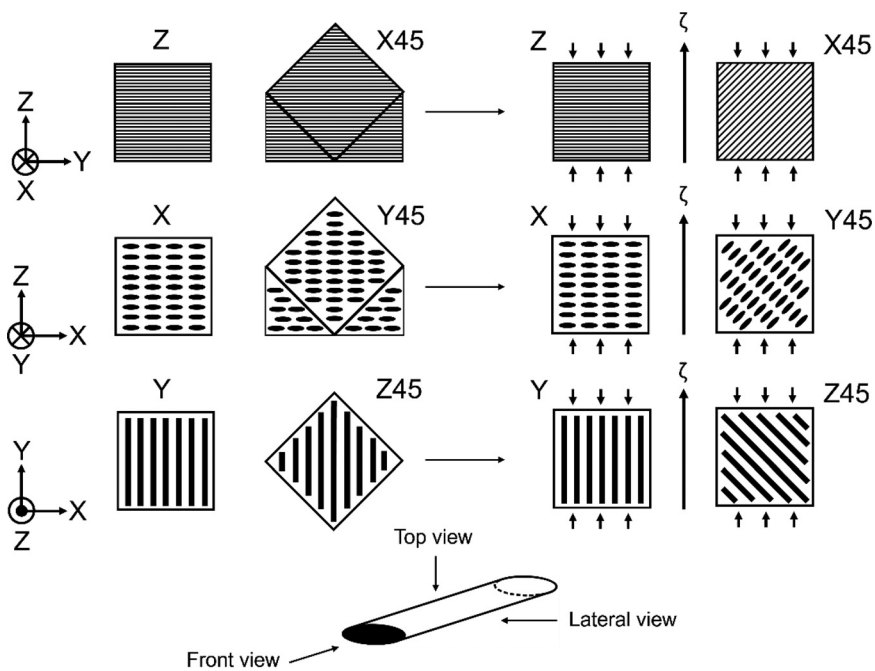

Notes: Thin lines represent the lateral faces of rasters, while thick lines represent the top faces of rasters. Ellipsoidal shapes show the starting (or finishing) points of the deposition of rasters. Thick black lines highlight the geometrical shapes of the specimens where supports are replaced by bulk material. Details of a single raster are also presented, in the 0° printing configuration the lateral view coincides with the X direction, the front view with the Y direction and the top view with the Z direction

Source: Figure by authors

Figure 8 FE model of the compression test in LS-DYNA environment

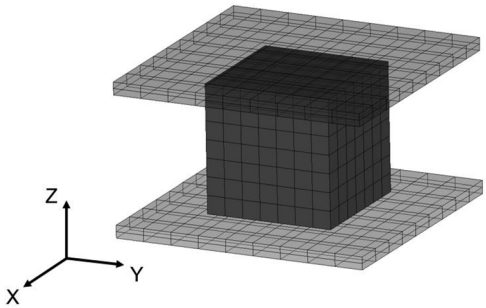

Source: Figure by authors

description of the elastic phase and a yield criterion with a contextual hardening law for the evolution in the plastic region (Zouaoui *et al.*, 2021; Bandinelli *et al.*, 2023; Kucewicz *et al.*, 2018; Bhandari *et al.*, 2020). For as the elastic phase is concerned, an orthotropic elastic matrix is considered to describe the material's behaviour. In particular, nine independent elastic constants are needed to fully characterize the material's orthotropy: the elastic moduli in the three main material's directions (X, Y and Z), the elastic shear moduli in the planes identified by the three main directions and three Poisson's ratios. Elastic moduli of X, Y and Z directions are derived from experimental values, as well as three out of six Poisson's ratios. Shear elastic moduli are evaluated by comparing trends of experimental and numerical elastic moduli with respect to the material's orientation. In this sense, the latter is calculated by equation (1), usually adopted for composite materials (Daniel, 2006):

$$E_{\zeta,th} = \left(\frac{1}{E_{ii}}\cos^4\theta + \left(\frac{1}{G_{ji}} - \frac{2\nu_{ij}}{E_{ii}}\right)\sin^2\theta\cos^2\theta + \frac{1}{E_{jj}}\sin^4\theta\right)^{-1} \quad (1)$$

where ζ indicates the direction of load application as shown in Figure 7. The letter ζ indicates the angle between the specific material's direction and the load direction ζ, so a 0° angle corresponds to E_{ii} while a 90° angle corresponds to E_{jj}. Shear elastic moduli are then numerically evaluated by minimizing differences between experimental and theoretical values of elastic moduli in the different building angles. The remaining Poisson's ratios are found thanks to the symmetry of the elastic matrix by means of equation (2):

$$\frac{\nu_{ij}}{E_{ii}} = \frac{\nu_{ji}}{E_{jj}} \quad (2)$$

For what the transition between the elastic and the plastic regimes is concerned, the material's behaviour is modelled through Hill's anisotropic yield criterion (Hill, 1948):

$$F(\sigma_{yy} - \sigma_{zz})^2 + G(\sigma_{zz} - \sigma_{xx})^2 + H(\sigma_{xx} - \sigma_{yy})^2 + 2L\tau_{yz}^2 + 2M\tau_{xz}^2 + 2N\tau_{xy}^2 = 1 \quad (3)$$

where the subscripts of stresses in equation (3) refer to the material reference system described in Figure 1. As already stated in Bandinelli *et al.*(2023); Colby (2013), Hill's parameters F, G, H, L, M and N do not only define the

Table 4 Material properties adopted in the FE simulations in the LS-DYNA environment for the case of 0° raster angle, in the general orthotropic configuration

E_{xx} (MPa)	E_{yy} (MPa)	E_{zz} (MPa)	G_{xy} (MPa)	G_{xz} (MPa)	G_{yz} (MPa)
1,400	2,530	1,500	570	505	470
ν_{xy} (−)	ν_{yx} (−)	ν_{xz} (−)	ν_{zx} (−)	ν_{yz} (−)	ν_{zy} (−)
0.115	0.208	0.400	0.429	0.250	0.149
F (1/MPa^2)	G (1/MPa^2)	H (1/MPa^2)	L (1/MPa^2)	M (1/MPa^2)	N (1/MPa^2)
0.000135	0.000494	0.000299	0.001422	0.001303	0.001295
C_r (−)	Q_r (−)	C_{rs} (−)	Q_{rs} (−)		
4.028	0.474	0.001	8.097		

Source: Table by authors

Table 5 Material properties adopted in the FE simulations in the LS-DYNA environment for the case of 0° raster angle, in the transversely isotropic configuration

E_{xx} (MPa)	E_{yy} (MPa)	E_{zz} (MPa)	G_{xy} (MPa)	G_{xz} (MPa)	G_{yz} (MPa)
1,450	2,530	1,450	550	510	510
ν_{xy} (−)	ν_{yx} (−)	ν_{xz} (−)	ν_{zx} (−)	ν_{yz} (−)	ν_{zy} (−)
0.144	0.250	0.400	0.400	0.250	0.144
F (1/MPa^2)	G (1/MPa^2)	H (1/MPa^2)	L (1/MPa^2)	M (1/MPa^2)	N (1/MPa^2)
0.000214	0.000466	0.000214	0.00141	0.00139	0.00141
C_r (−)	Q_r (−)	C_{rs} (−)	Q_{rs} (−)		
4.263	0.463	0.033	0.418		

Source: Table by authors

transition between elastic and plastic phases, but they also drive the subsequent one, where the plastic behaviour is described through the evolution of the yield surface. In a purely experimental approach, the elastic limits evaluated by compression tests represent the yield value to be used in Hill's anisotropic yield criterion but could not be representative of the whole plastic behaviour. The use of optimization software helps consider the entire post-yielding phase of the behaviour,

Table 6 Material's properties adopted in the FE simulations in the LS-DYNA environment for the case of 0°/45°/90°/135° stacking sequence

E_{xx} (MPa)	E_{yy} (MPa)	E_{zz} (MPa)	G_{xy} (MPa)	G_{xz} (MPa)	G_{yz} (MPa)
1,720	1,720	1,530	605	400	400
ν_{xy} (−)	ν_{yx} (−)	ν_{xz} (−)	ν_{zx} (−)	ν_{yz} (−)	ν_{zy} (−)
0.320	0.320	0.400	0.356	0.400	0.356
F (1/MPa^2)	G (1/MPa^2)	H (1/MPa^2)	L (1/MPa^2)	M (1/MPa^2)	N (1/MPa^2)
0.000430	0.000430	0.000425	0.00207	0.00207	0.00122
C_r (−)	Q_r (−)	C_{rs} (−)	Q_{rs} (−)		
3.701	0.554	0.035	1.050		

Source: Table by authors

Figure 9 Comparisons between experimental (squared markers) and numerical distributions (continuous lines for the generic orthotropic model and dashed lines for the transversely isotropic ones) of elastic moduli in the 0° configuration (on the left) and in the 0°/45°/90°/135° configuration (on the right)

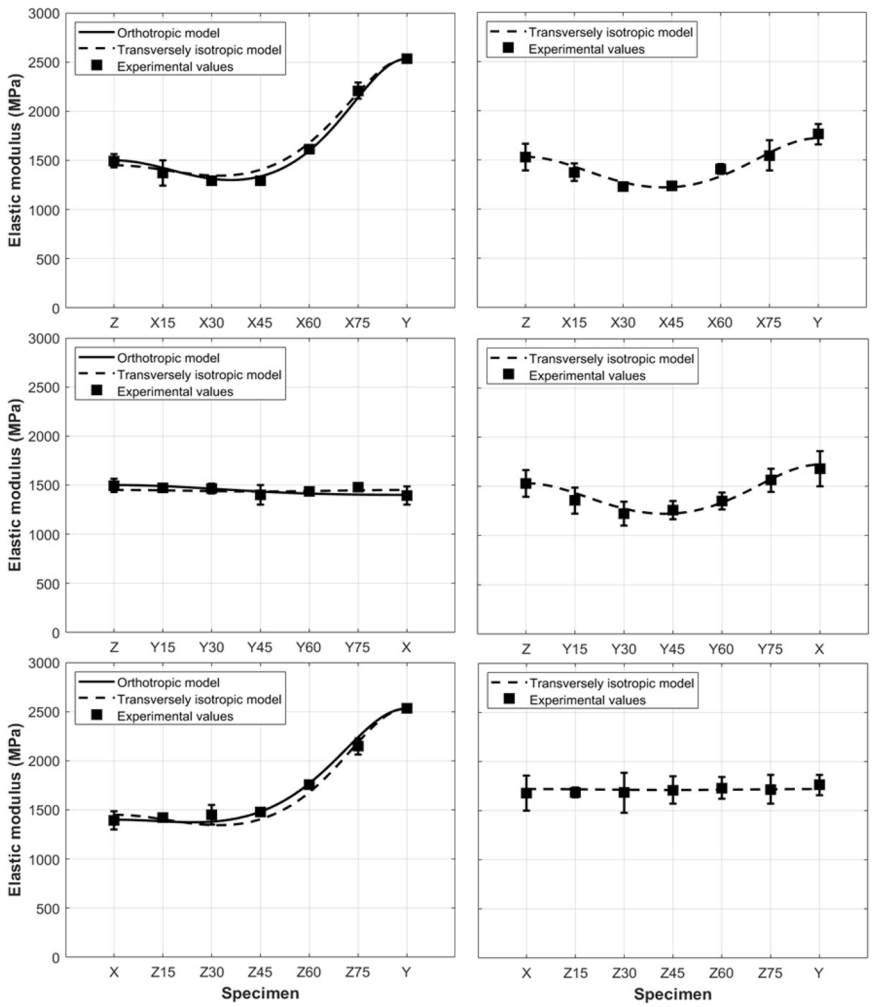

Notes: The top images show trends of specimens progressively rotated around the x-axis, the middle images show those of the y-axis, and the bottom images show those of the z-axis
Source: Figure by authors

leading to more representative parameters. The hardening phase is then modelled with Voce's isotropic hardening law (equation (4)) (Voce, 1948) so that the stresses in the different material's directions are driven by a unique curve that links equivalent stress to equivalent plastic strain:

$$\sigma\left(\varepsilon_{eq}^{p}\right) = \sigma_0 + Q_{r1}\left[\left(1 - exp\left(-C_{r1}\varepsilon_{eq}^{p}\right)\right)\right] + Q_{r2}\left[\left(1 - exp\left(-C_{r2}\varepsilon_{eq}^{p}\right)\right)\right] \quad (4)$$

where Q_{r1}, Q_{r2}, C_{r1} and C_{r2} are Voce's parameters. The individuation of the hardening law requires the knowledge of the formulation of the equivalent plastic strain, which is quite an expensive computation for an anisotropic material such as the one analysed in the present work (Zhang *et al.*, 2018). The calculation is assigned to the FE software and the hardening curve is found by means of an optimization procedure in LS-OPT software, that adjusts Hill's and Voce's parameters to have the best numerical fit between experimental and FE load-displacement curves.

Figure 10 Comparisons between experimental and numerical (orthotropic model) engineering stress–strain curves of the 0° configuration

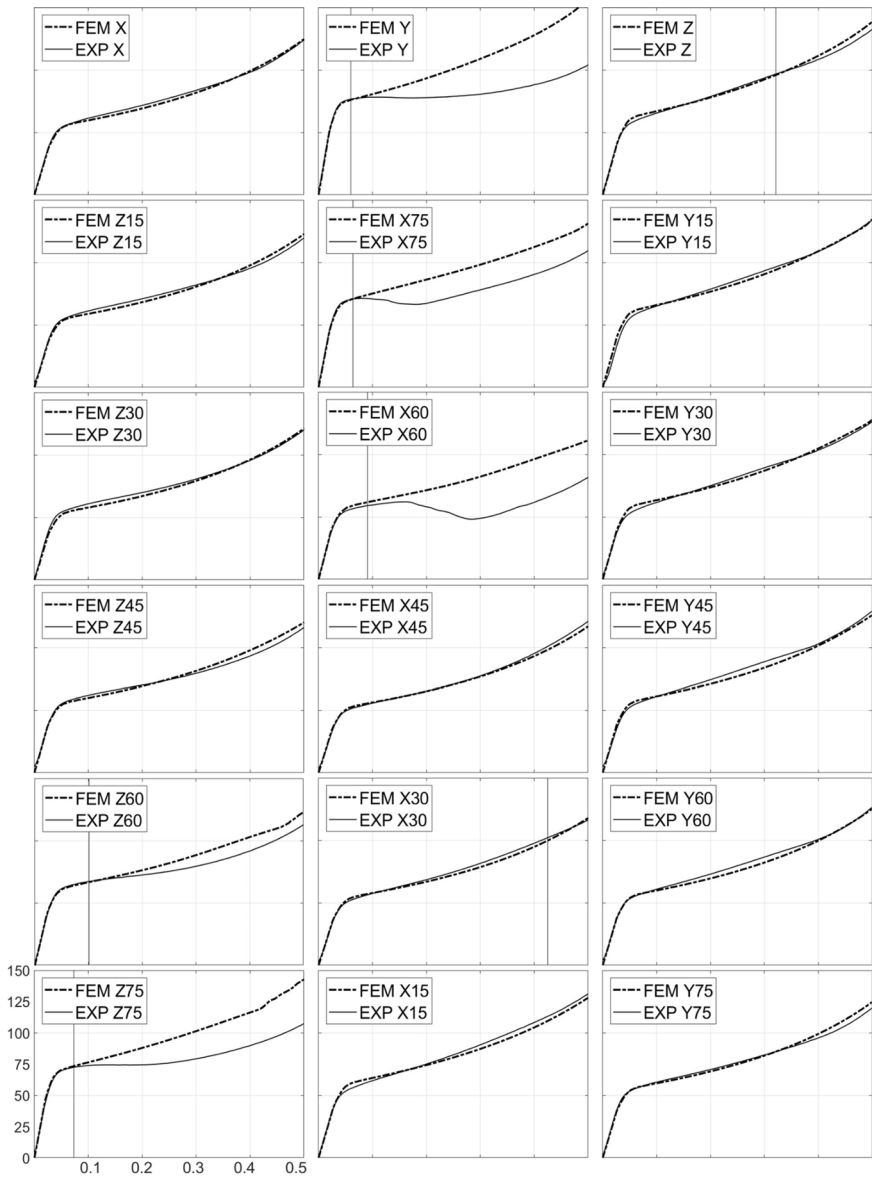

Notes: The vertical scale is expressed in MPa, while the horizontal one is dimensionless. Where present, vertical continuous lines represent the limit of validity of the FE model, so the point from which the true uniaxial compressive stress starts to decrease
Source: Figure by authors

4.2 Finite element model

From experimental observations different hypotheses are made about the material model used in the FEA: the 0° configuration is represented with the assumptions of both a generic orthotropic model and a transversely isotropic one (with X and Z directions considered equal), while the 0°/45°/90°/135° configuration is represented by a transversely isotropic model only (with X and Y directions considered equal).

The FE analysis is conducted to represent the material's compressive behaviour in the test condition. In this sense, a FE model is built inside the LS-DYNA environment to simulate the compression tests on all the specimens. For each specimen 343 ($7 \times 7 \times 7$) fully integrated solid elements are used, while 162 ($2 \times 9 \times 9$) constant stress solid elements are used for each of the two rigid plates that are used to apply the compressive load. Between the latter, one is fixed in space, while a prescribed motion of 6 mm is imposed on the other (Figure 8). An anisotropic elasto-plastic material model (MAT 157) is used to model the printed material, as it accounts for anisotropy both in elastic and plastic regimes, whereas a rigid elastic material (MAT 020) is used to model the testing machine's steel plates. Material's orientation in space is accounted for by specific parameters of MAT157's card, where a global material's coordinate system is specified, so each specimen has its own while the geometry of the simulation is kept equal. A

Figure 11 Comparisons between experimental and numerical engineering stress–strain curves of the 0°/45°/90°/135° configuration

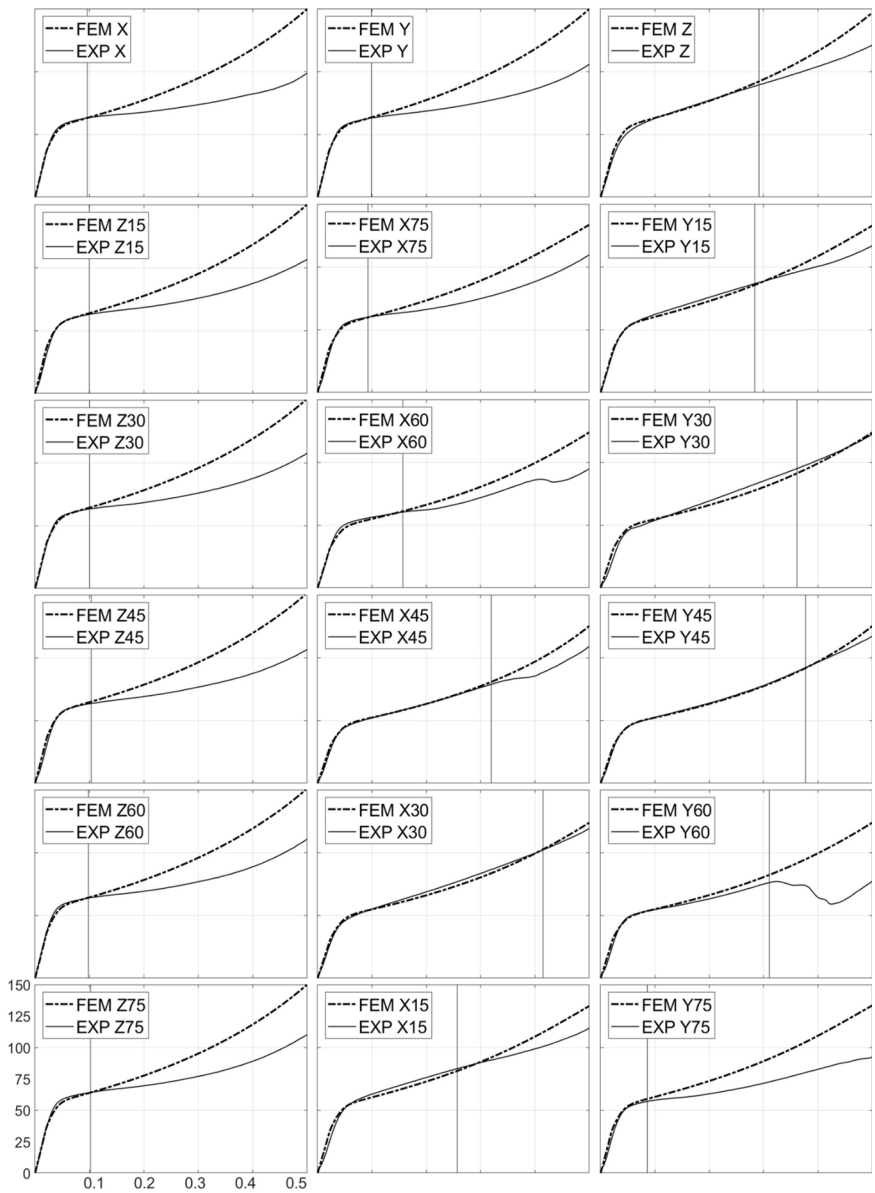

Notes: The vertical scale is expressed in MPa, while the horizontal one is dimensionless. Where present, vertical continuous lines represent the limit of validity of the FE model, so the point from which the true uniaxial compressive stress starts to decrease
Source: Figure by authors

node-to-surface contact is added to transfer load, with a friction coefficient of 0.08.

Tables 4 and 5 report the material's properties used for the simulations in the case of 0° raster angle in both the general orthotropic configuration and transversely isotropic configuration, respectively.

Table 6 reports the material's properties used for the simulations in the case of 0°/45°/90°/135° raster angle stacking sequence, considering a transversely isotropic material model.

5. Results and discussion

The following analysis compares experimental and numerical material properties as well as engineering stress–strain curves and deformed shapes at the end of the compression tests.

5.1 Elastic behaviour

Experimental and numerical elastic moduli of the 0° and 0°/45°/90°/135° configurations are presented in Figure 9, showing good fitting of the material models used. Here continuous and dashed curves represent numerical values of the compressive elastic modulus and its dependence on the material's orientation is derived from equation (1) which exactly reflects values of the FE simulations (Zhao *et al.*, 2019; Daniel, 2006). For as the 0° configuration is concerned, the generic orthotropic elastic model can better represent the trend of elastic moduli (with a maximum error of 5.09% of specimen Y75), but the

Figure 12 Comparisons between experimental and FE trends of engineering stress with respect to specimens' orientation

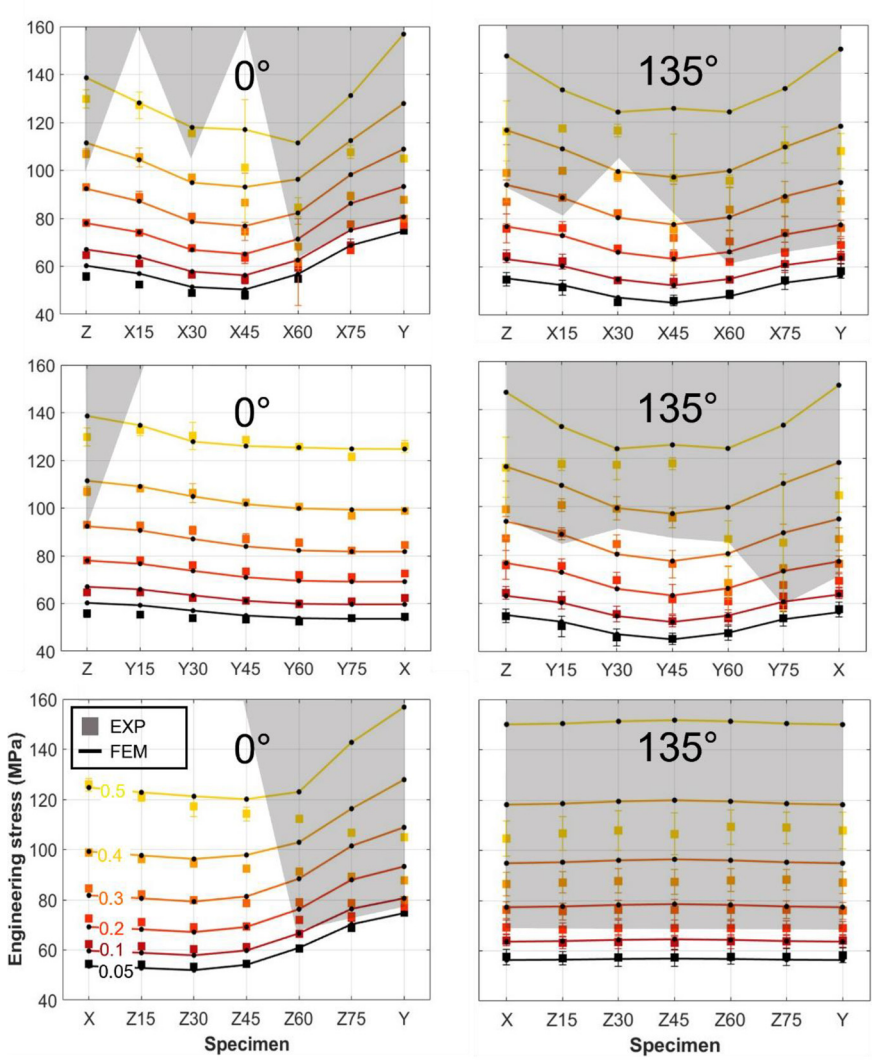

Notes: Different levels of engineering strain are evaluated and are indicated with different colors in the legend (0.05, 0.1, 0.2, 0.3, 0.4, 0.5). FE trends are represented with continuous lines, while experimental values are depicted by square markers. The grey area in the graphs represents the region in which the comparison does not hold due to damage and failure of specimens (as discussed in Section 5.2)

Source: Figure by authors

assumption of a transversely isotropic model is considered acceptable, as the maximum deviation between experimental and numerical moduli is 8.9% (specimen X45). Observing trends of the 0°/45°/90°/135° configuration, the hypothesis of a transversely isotropic model appears more appropriate as specimens rotating around the z-axis present almost identical elastic moduli, and the two remaining trends are almost overlapping. It can be noted that in the 0° configuration, the isotropic plane appears to be XZ, while in the 0°/45°/90°/135° configuration it appears to be XY.

5.2 Plastic behaviour

As previously discussed, the FE model is generated to describe the plastic behaviour of the material, adopting Hill's yield criterion and Voce's isotropic hardening law. In this work, neither damage nor failure are analysed using FE, but a phenomenological discussion is given in the following. This said the authors choose to identify the onset of damage mechanisms with the decrease in true uniaxial compressive stress and restrict the validity of the comparison between FE models and experimental data accordingly. Figures 10 and 11 display a comparison between curves of the experimental and FE analyses in the cases of the 0° (comparison with the orthotropic model only) and 0°/45°/90°/135° configurations, respectively, showing good accuracy in representing the plastic behaviour of the material in the range of validity. This is further motivated by the fact that a single material model (one for each printing configuration) can describe the material's behaviour in 18 different cases, which represent various relative orientations between loading and the material's directions. The experimental curves shown are selected by being the closest to the corresponding mean curves. The experimental curves display once again the significant difference between the two printing configurations, showing how the 0°/45°/90°/135° stacking sequence is more prone to damage and failure. In the 0° configuration, only 5 specimens out of 18 (X60, X75, Y, Z60, Z75) are prone to failure, whereas others show almost no sign of a decrease in true uniaxial compressive stress.

Figure 12 displays comparisons between experimental and FE results with engineering stress evaluated at different engineering strains, where the first are mean values of the corresponding tests. This comparison shows a good agreement between the experimental and numerical values considering the range of validity of the model (the grey background represents strain levels at which the onset of damage occurred, therefore the region in which the presented model has no validity).

FE models are also able to capture an accurate representation of the deformed shapes of some specimens. Figure 13 shows the comparison between numerical and experimental deformed shapes for some of the specimens:

The numerical model is not able to capture deformed shapes when damage and failure mechanisms occur but

Figure 13 Comparison between numerical and experimental deformed shapes, with values of effective strain

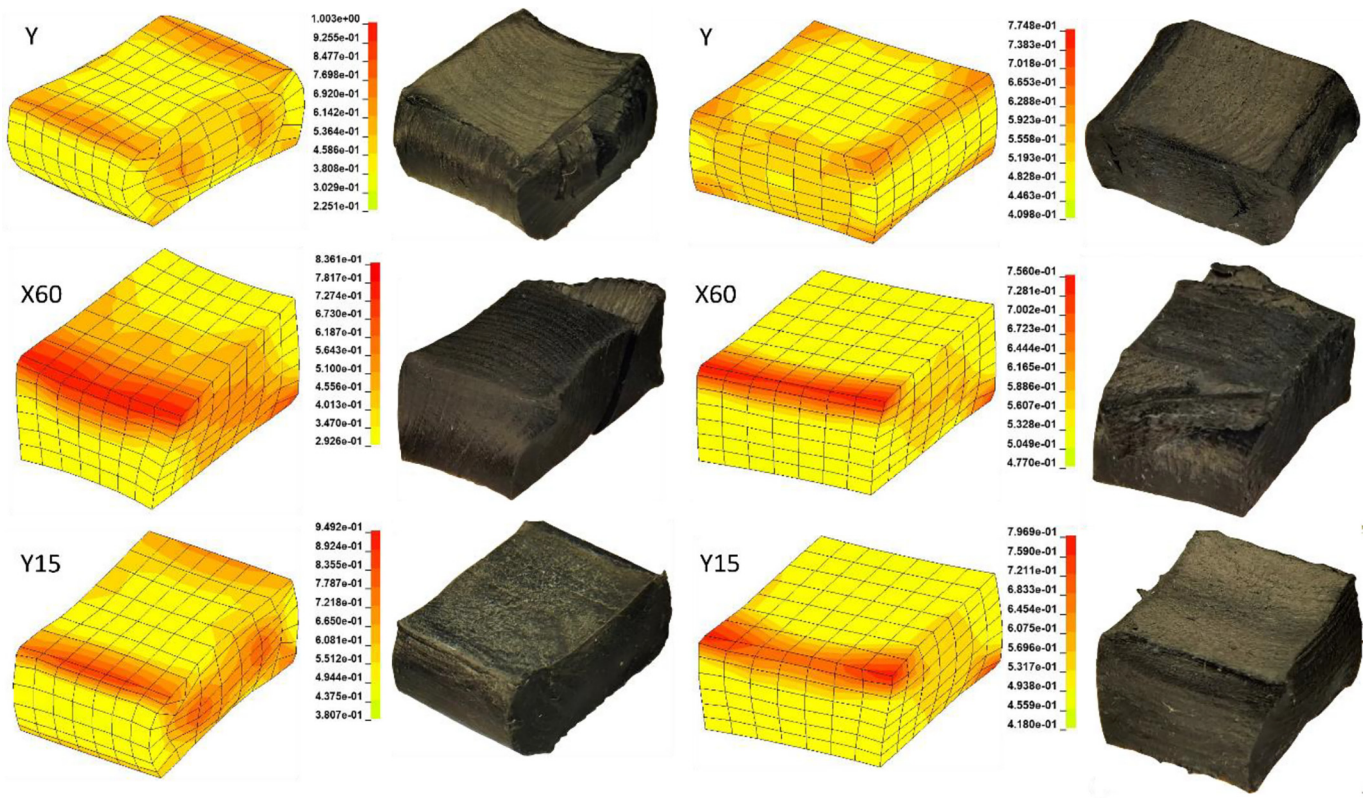

Note: Specimens of the 0° and 0°/45°/90°/135° printing configurations are depicted on the left and right side of the image, respectively
Source: Figure by authors

accounts for the anisotropic nature of the material; in fact, the model does not represent the damage and failure mechanisms and therefore fails to capture this type of behaviour. As an example, specimens X60 show premature failure for both stacking sequences of raster angles, so their deformed shape cannot be entirely represented by the FE model. It is interesting to notice the difference in final shapes between the same specimens of the two different printing configurations, both in FE models and experimental pictures, that highlights the effect of the stacking sequence of raster angles.

5.3 Damage and failure

In this section, a phenomenological discussion about damage and failure mechanisms observed during compression tests is proposed. In the case of the 0° configuration, considerable damage is observed for the Y specimen, which has the highest stiffness and where the Z direction is perpendicular to the loading direction. Specimens Y, as already observed in Zeybek *et al.* (2023), show two perpendicular shear bands that drive the opening of a central crack (as shown in Figure 14). Specimens X show a deformation behaviour driven by the separation between layers, along the Z direction, but do not reach a failure condition. The specimens tested along the Z direction show a transversal deformation behaviour that is mainly driven by the stretching of the raster's interfaces along the X direction, but again no failure condition is reached.

Figure 14 Shear bands (dashed white lines) and central crack opening (white circle) observed in the Y specimens of the 0° printing configuration

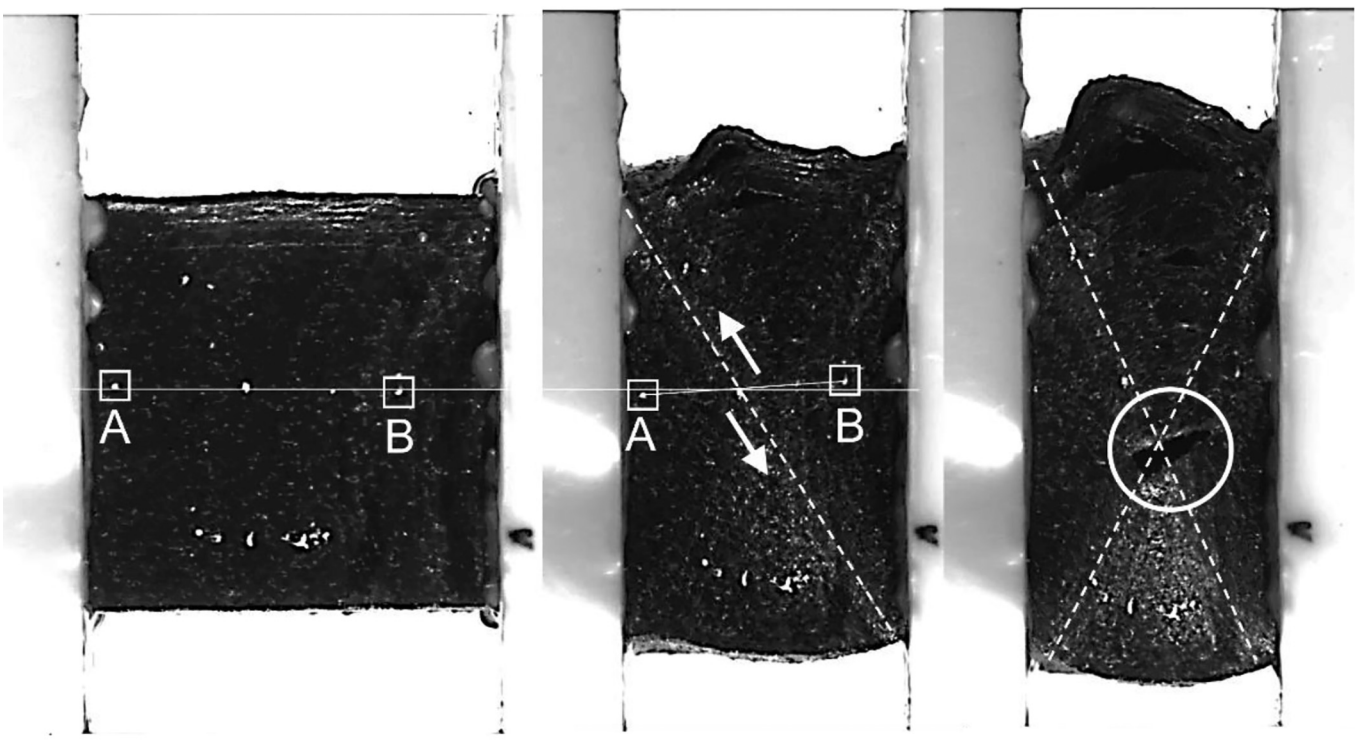

Note: Points A and B (white paint marks highlighted with square boxes) move according to a shear sliding of the specimen (shown by white arrows), as can be observed with the help of the thin continuous white lines
Source: Figure by authors

Figure 15 Shear deformation mechanism and failure of the X60 specimen in the 0° configuration

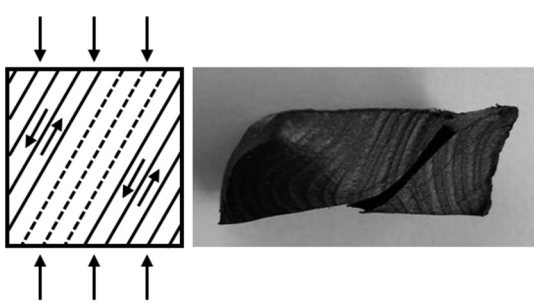

Note: Dashed lines represent printed layers that encounter greater resistance to shear sliding due to being constrained between both plates of the testing machine
Source: Figure by authors

Specimens X60, X75, Z60 and Z75 are the closest in terms of orientation to the Y specimens and are in fact characterized by high stiffness. Their orientation in space facilitates damage because printed layers are favourably aligned for delamination and shear sliding (Figure 15), but only X60 and Z75 show failure mechanisms: shear sliding and delamination of printed layers respectively. Other specimens do not show signs of failure, except for X45 and Y75 specimens that presented signs of shear failure in only one test.

In the case of the 0°/45°/90°/135° configuration, many specimens are subjected to damage and premature failure, with interlayer delamination being the principal cause (Guessasma

et al., 2016), followed by shear failure where the printed layers are favourably oriented. Specimens X, Y, Z15, Z30, Z45, Z60, and Z75 showed the first failure mode in all tests because the printed layers are always perpendicular to the load direction. Specimens X45, X60, X75, Y45, Y60 and Y75 showed the second failure mode in all tests (except for one Y45 specimen) because the printed layers are favourably oriented to shear sliding. The explanation for the 0°/45°/90°/135° configuration being more prone to failure is found in the deposition pattern, in fact, rasters crossing with different orientations promote the formation of voids and enhance residual stresses, decreasing the layer adhesion strength (Khan *et al.*, 2022; Turner *et al.*, 2014).

Damage and failure mechanisms strongly depend on material orientation, so an anisotropic criterion should be considered to model the material's failure behaviour. In the present work, an isotropic hardening law is used to represent the plastic evolution, so there is no possibility of describing the anisotropic nature of the material's failure.

6. Conclusions

3D-printed material's characterization is not an easy task, and its anisotropic nature poses many challenges from the behaviour modelling point of view. Most of the literature works focus on the tensile characterization of printed materials, leaving their compression behaviour unsolved. Compression tests are a useful tool to characterize FFF material's behaviour and the use of post-processed specimens (presented herein) allows for a more representative study of the mechanical properties. The present work delivers an effective procedure to characterize the compressive behaviour of 3D-printed materials, focusing the attention on the post-processing of specimens and the FE modelling technique. No work to date, to the authors' knowledge, has explored a more complete combination of raster angles and building orientations, making this work valuable as a reference for anisotropy studies in the field of 3D-printed materials. Among different findings, the present work highlighted the dependency of mechanical behaviour (both elasto-plastic behaviour and failure modes) on both building strategy and orientation in space. The material model based on an elastic stiffness matrix with a combination of Hill's yield criterion and Voce's isotropic hardening law is able to represent the short carbon-reinforced PA12 anisotropic behaviour, also capturing some aspects of the deformation modes. Once enriched with a failure criterion, the FE model can be effectively used for verification and design purposes. Future work will be conducted to deepen the understanding of failure modes and novel material's characterization techniques.

References

Athale, M., Park, T., Hahnlen, R. and Pourboghrat, F. (2022), "Experimental characterization and finite element simulation of FDM 3D printed polymer composite tooling for sheet metal stamping", *The International Journal of Advanced Manufacturing Technology*, Vol. 121 Nos 9/10, pp. 6973-6989, doi: 10.1007/s00170-022-09801-0.

Bandinelli, F., Peroni, L. and Morena, A. (2023), "Elasto-plastic mechanical modeling of fused deposition 3D printing materials".

Bandinelli, F., Peroni, L. and Scapin, M. (2024), "Experimental investigation of 3D printed infill structures for crash absorbing applications".

Bhandari, S., Lopez-Anido, R.A., Wang, L. and Gardner, D.J. (2020), "Elasto-plastic finite element modeling of short carbon fiber reinforced 3D printed acrylonitrile butadiene styrene composites", *JOM*, Vol. 72 No. 1, pp. 475-484, doi: 10.1007/s11837-019-03895-w.

Bikas, H., Stavropoulos, P. and Chryssolouris, G. (2016), "Additive manufacturing methods and modeling approaches: a critical review", *The International Journal of Advanced Manufacturing Technology*, Vol. 83 Nos 1/4, pp. 389-405, doi: 10.1007/s00170-015-7576-2.

Birosz, M.T., Andó, M. and Safranyik, F. (2022), "Layer adhesion test of additively manufactured pins: a shear test", *Polymers (Basel)*, Vol. 14 No. 1, doi: 10.3390/polym14010055.

Buj-Corral, I., Domínguez-Fernández, A. and Durán-Llucià, R. (2019), "Influence of print orientation on surface roughness in fused deposition modeling (FDM) processes", *Materials (Basel)*, Vol. 12 No. 23, p. 3834, doi: 10.3390/ma12233834.

Calignano, F., Lorusso, M., Roppolo, I. and Minetola, P. (2020), "Investigation of the mechanical properties of a carbon fibre-reinforced nylon filament for 3d printing", *Machines*, Vol. 8 No. 3, pp. 1-13, doi: 10.3390/machines8030052.

Cattenone, A., Morganti, S., Alaimo, G. and Auricchio, F. (2019), "Finite element analysis of additive manufacturing based on fused deposition modeling: distortions prediction and comparison with experimental data", *Journal of Manufacturing Science and Engineering*, Vol. 141 No. 1, doi: 10.1115/1.4041626.

Chacón, J.M., Caminero, M.A., García-Plaza, E. and Núñez, P.J. (2017), "Additive manufacturing of PLA structures using fused deposition modelling: effect of process parameters on mechanical properties and their optimal selection", *Mater. Des*, Vol. 124, pp. 143-157, doi: 10.1016/j.matdes.2017.03.065.

Colby, R.B. (2013), "Equivalent plastic strain for the hill's yield criterion under general three-dimensional".

Corvi, A., Collini, L., Sciancalepore, C. and Kumar, A. (2023), "Analysis and modelling of damage mechanism in FDM 3D-printed lattice structure under compression loading", *Journal of Mechanical Science and Technology*, Vol. 37 No. 3, doi: 10.1007/s12206-022-2104-4.

Daniel, I.M. (2006), "Engineering mechanics of composite materials Ori Lshai".

Dong, G., Tang, Y. and Zhao, Y.F. (2017), "A survey of modeling of lattice structures fabricated by additive manufacturing", *Journal of Mechanical Design*, Vol. 139 No. 10, pp. 1-13, doi: 10.1115/1.4037305.

Dudescu, C. and Racz, L. (2017), "Effects of raster orientation, infill rate and infill pattern on the mechanical properties of 3D printed materials", *ACTA Universitatis Cibiniensis*, Vol. 69 No. 1, pp. 23-30, doi: 10.1515/aucts-2017-0004.

Fallon, J.J., McKnight, S.H. and Bortner, M.J. (2019), "Highly loaded fiber filled polymers for material extrusion: a review of current understanding", *Additive Manufacturing*, Vol. 30, p. 100810, doi: 10.1016/j.addma.2019.100810.

Fang, L., *et al.* (2021), "Estimations of the effective young's modulus of specimens prepared by fused filament

fabrication", *Additive Manufacturing*, Vol. 42, p. 101983, doi: 10.1016/j.addma.2021.101983.

Ferreira, I., Melo, C., Neto, R., Machado, M., Alves, J.L. and Mould, S. (2020), "Study of the annealing influence on the mechanical performance of PA12 and PA12 fibre reinforced FFF printed specimens", *Rapid Prototyping Journal*, Vol. 26 No. 10, pp. 1761-1770, doi: 10.1108/RPJ-10-2019-0278.

Ferrell, W.H., Clement, J. and TerMaath, S. (2021), "Uniaxial tensile testing standardization for the qualification of fiber reinforced plastics for fused filament fabrication", *Mechanics of Advanced Materials and Structures*, Vol. 28 No. 12, pp. 1254-1273, doi: 10.1080/15376494.2019.1660438.

Garg, A. and Bhattacharya, A. (2016), "An insight to the failure of FDM parts under tensile loading_ finite element analysis and experimental study", *Int. J. Mech. Sci*, Vol. 120, pp. 225-236, doi: 10.1016/j.ijmecsci.2016.11.032.

Ginoux, G., Paux, J. and Allaoui, S. (2023), "New preparation method of microstructurally and mechanically standardized PETG specimens by material extrusion additive manufacturing and machining", *Additive Manufacturing*, Vol. 66, p. 103471, doi: 10.1016/j.addma.2023.103471.

Gonabadi, H., Yadav, A. and Bull, S.J. (2020), "The effect of processing parameters on the mechanical characteristics of PLA produced by a 3D FFF printer", doi: 10.1007/s00170-020-06138-4/Published.

Guessasma, S., Belhabib, S., Nouri, H. and Ben Hassana, O. (2016), "Anisotropic damage inferred to 3D printed polymers using fused deposition modelling and subject to severe compression", *European Polymer Journal*, Vol. 85, pp. 324-340, doi: 10.1016/j.eurpolymj.2016.10.030.

Heller, B.P., Smith, D.E. and Jack, D.A. (2016), "Effects of extrudate swell and nozzle geometry on fiber orientation in fused filament fabrication nozzle flow", *Additive Manufacturing*, Vol. 12, pp. 252-264, doi: 10.1016/j.addma.2016.06.005.

Hill. (1948), "A theory of the yielding and plastic flow of anisotropic metals", *Proc. R. Soc. London. Ser. A. Math. Phys. Sci*, Vol. 193 No. 1033, pp. 281-297, doi: 10.1098/rspa.1948.0045.

Kannan, S., Vezhavendhan, R., Kishore, S. and Kanumuru, K.V. (2020), "Investigating the effect of orientation, infill density with triple raster pattern on the tensile properties for 3D printed samples", *IOP SciNotes*, Vol. 1 No. 2, p. 24405, doi: 10.1088/2633-1357/abb290.

Khan, S., Joshi, K. and Deshmukh, S. (2022), "Materials today: proceedings a comprehensive review on effect of printing parameters on mechanical properties of FDM printed parts", *Materials Today: Proceedings*, Vol. 50, pp. 2119-2127, doi: 10.1016/j.matpr.2021.09.433.

Kucewicz, M., Baranowski, P., Małachowski, J., Popławski, A. and Płatek, P. (2018), "Modelling, and characterization of 3D printed cellular structures", *Materials & Design*, Vol. 142, pp. 177-189, doi: 10.1016/j.matdes.2018.01.028.

Livermore Software Technology Corporation (LSTC) (2012), "keyword user' S manual", vol. I, no. August.

Love, L.J., *et al.* (2014), "The importance of carbon fiber to polymer additive manufacturing", *Journal of Materials Research*, Vol. 29 No. 17, pp. 1893-1898, doi: 10.1557/jmr.2014.212.

Mulholland, T., Goris, S., Boxleitner, J., Osswald, T.A. and Rudolph, N. (2018), "Process-induced fiber orientation in fused filament fabrication", *Journal of Composites Science*, Vol. 2 No. 3, pp. 1-14, doi: 10.3390/jcs2030045.

Ning, F., Cong, W., Qiu, J., Wei, J. and Wang, S. (2015), "Additive manufacturing of carbon fiber reinforced thermoplastic composites using fused deposition modeling", *Composites Part B: Engineering*, Vol. 80, pp. 369-378, doi: 10.1016/j.compositesb.2015.06.013.

Paul, S. (2021), "Finite element analysis in fused deposition modeling research: a literature review", *Measurement*, Vol. 178, doi: 10.1016/j.measurement.2021.109320.

Peng, C., Tran, P. and Mouritz, A.P. (2022), "Compression and buckling analysis of 3D printed carbon fibre-reinforced polymer cellular composite structures", *Composite Structures*, Vol. 300 No. April, p. 116167, doi: 10.1016/j.compstruct.2022.116167.

Phillips, C., Kortschot, M. and Azhari, F. (2022), "Towards standardizing the preparation of test specimens made with material extrusion: review of current techniques for tensile testing", *Additive Manufacturing*, Vol. 58 No. July, p. 103050, doi: 10.1016/j.addma.2022.103050.

Reddy, V., Flys, O., Chaparala, A., Berrimi, C.E., Amogh, V. and Rosen, B.G. (2018), "Study on surface texture of fused deposition modeling", *Procedia Manufacturing*, Vol. 25, pp. 389-396, doi: 10.1016/j.promfg.2018.06.108.

Retolaza, J., Ansola, R., Gómez, J.L. and Díez, G. (2021), "Identifying elastic constants for pps technical material when designing and printing parts using fdm technology", *Materials (Basel)*, Vol. 14 No. 5, pp. 1-19, doi: 10.3390/ma14051123.

Samy, A.A., *et al.* (2022), "Influence of raster pattern on residual stress and part distortion in FDM of semi-crystalline polymers: a simulation study", *Polymers (Basel)*, Vol. 14 No. 13, doi: 10.3390/polym14132746.

Scapin, M. and Peroni, L. (2021), "Numerical simulations of components produced by fused deposition 3D printing", *Materials (Basel)*, Vol. 14 No. 16, doi: 10.3390/xxxxx.

Sola, A., *et al.* (2023), "Open challenges in tensile testing of additively manufactured polymers: a literature survey and a case study in fused filament fabrication", *Polymer Testing*, Vol. 117, p. 107859, doi: 10.1016/j.polymertesting.2022.107859.

Song, Y., Li, Y., Song, W., Yee, K., Lee, K. and Tagarielli, V.L. (2017), "Measurements of the mechanical response of unidirectional 3D-printed PLA", *Materials & Design*, Vol. 123, pp. 154-164, doi: 10.1016/j.matdes.2017.03.051.

Sood, A.K., Ohdar, R.K. and Mahapatra, S.S. (2012), "Experimental investigation and empirical modelling of FDM process for compressive strength improvement", *Journal of Advanced Research*, Vol. 3 No. 1, pp. 81-90, doi: 10.1016/j.jare.2011.05.001.

Sood, A.K., Ohdar, R.K. and Mahapatra, S.S. (2009), "Improving dimensional accuracy of fused deposition modelling processed part using grey Taguchi method", *Materials & Design*, Vol. 30 No. 10, pp. 4243-4252, doi: 10.1016/j.matdes.2009.04.030.

Stander, N.A. *et al.* (2019), "LS-OPT user ' s manual: a design optimization and probabilistic analysis tool for the engineering analyst", no. February.

Sun, Q. (2008), "Effect of processing conditions on the bonding quality of FDM polymer filaments", *Rapid Prototyping Journal*, Vol. 14 No. 2, pp. 72-80, doi: 10.1108/13552540810862028.

Tabacu, S. and Ducu, C. (2020), "Numerical investigations of 3D printed structures under compressive loads using damage and fracture criterion: experiments, parameter identification, and validation", *Extreme Mechanics Letters*, Vol. 39, p. 100775, doi: 10.1016/j.eml.2020.100775.

Tekinalp, H.L., *et al.* (2014), "Highly oriented carbon fiber – polymer composites via additive manufacturing", *Composites Science and Technology*, Vol. 105, pp. 144-150, doi: 10.1016/j.compscitech.2014.10.009.

Tessarin, A., Zaccariotto, M., Galvanetto, U. and Stocchi, D. (2022), "A multiscale numerical homogenization-based method for the prediction of elastic properties of components produced with the fused deposition modelling process", *Results Eng*, Vol. 14, p. 100409, doi: 10.1016/j.rineng.2022.100409.

Trofimov, A., Le Pavic, J., Pautard, S., Therriault, D. and Lévesque, M. (2022), "Experimentally validated modeling of the temperature distribution and the distortion during the fused filament fabrication process", *Additive Manufacturing*, Vol. 54, p. 102693, doi: 10.1016/j.addma.2022.102693.

Turner, B.N., Strong, R. and Gold, S.A. (2014), "A review of melt extrusion additive manufacturing processes: I. Process design and modeling", *Rapid Prototyping Journal*, Vol. 20 No. 3, pp. 192-204, doi: 10.1108/RPJ-01-2013-0012.,

Voce, E. (1948), "The relationship between stress and strain for homogeneous deformation", *Journal of the Institute of Metals*, Vol. 74, pp. 537-562.

Wang, T.M., Xi, J.T. and Jin, Y. (2007), "A model research for prototype warp deformation in the FDM process", *The International Journal of Advanced Manufacturing Technology*, Vol. 33 Nos 11/12, pp. 1087-1096, doi: 10.1007/s00170-006-0556-9.

Wickramasinghe, S., Do, T. and Tran, P. (2020), "FDM-Based 3D printing of polymer and associated composite: a review on mechanical properties".

Yao, T., Ye, J., Deng, Z., Zhang, K. and Ma, Y. (2020), "Tensile failure strength and separation angle of FDM 3D printing PLA material: experimental and theoretical analyses", *Compos. Part B*, Vol. 188, p. 107894, doi: 10.1016/j.compositesb.2020.107894.

Yu, M., *et al.* (2023), "The effect of cooling rates on thermal, crystallization, mechanical and barrier properties of rotational molding polyamide 11 as the liner material for High-Capacity High-Pressure vessels", *Molecules*, Vol. 28 No. 6, p. 2425, doi: 10.3390/molecules28062425.

Yu, N., Sun, X., Wang, Z., Zhang, D. and Li, J. (2020), "Effects of auxiliary heat on warpage and mechanical properties in carbon fi ber/ABS composite manufactured by fused deposition modeling", *Materials & Design*, Vol. 195, p. 108978, doi: 10.1016/j.matdes.2020.108978.

Zeybek, M.K., Güden, M. and Taşdemirci, A. (2023), "The effect of strain rate on the compression behavior of additively manufactured short carbon Fiber-Reinforced polyamide composites with different layer heights, infill patterns, and built angles", *J. Mater. Eng. Perform*, p. 14, doi: 10.1007/s11665-023-07918-1.

Zhang, W., *et al.* (2018), "Interfacial bonding strength of short carbon fiber/acrylonitrile-butadiene-styrene composites fabricated by fused deposition modeling", *Composites Part B: Engineering*, Vol. 137, pp. 51-59, doi: 10.1016/j.compositesb.2017.11.018.

Zhao, Y., Chen, Y. and Zhou, Y. (2019), "Novel mechanical models of tensile strength and elastic property of FDM AM PLA materials: experimental and theoretical analyses", *Materials & Design*, Vol. 181, p. 108089, doi: 10.1016/j.matdes.2019.108089.

Ziemian, C., Sharma, M. and Ziemi, S. (2012), "Anisotropic mechanical properties of ABS parts fabricated by fused deposition modelling", *In Mechanical Engineering*.

Zouaoui, M., Gardan, J., Lafon, P., Makke, A., Labergere, C. and Recho, N. (2021), "A finite element method to predict the mechanical behavior of a pre-structured material manufactured by fused filament fabrication in 3D printing", *Applied Sciences*, Vol. 11 No. 11, doi: 10.3390/app11115075.

Further reading

Turner, B.N. and Gold, S.A. (2015), "A review of melt extrusion additive manufacturing processes: II. Materials, dimensional accuracy, and surface roughness", *Rapid Prototyping Journal*, Vol. 21 No. 3, pp. 250-261, doi: 10.1108/RPJ-02-2013-0017.

Corresponding author

Francesco Bandinelli can be contacted at: francesco.bandinelli@polito.it

For instructions on how to order reprints of this article, please visit our website:
www.emeraldgrouppublishing.com/licensing/reprints.htm
Or contact us for further details: **permissions@emeraldinsight.com**